Propagation Effects in Satellite Mounted Radar Remote Sensing

(Invited Paper)

Andreas Danklmayer
DLR e.V. (German Aerospace Center)
Microwaves and Radar Institute
82234 Wessling, Oberpfaffenhofen
Germany
Email: Andreas.Danklmayer@dlr.de

Abstract— Space-borne Synthetic Aperture Radar (SAR) imaging is often considered to possess both day/night and all weather operational capabilities. However, as the operating frequencies of SAR-systems are increasing, visible image distortions due to heavy precipitation in SAR-images may become present. This holds especially for the case of convective rain events imaged at X-band frequencies and beyond. These rain-cell signatures are thoroughly investigated, and the physical background of the related propagation effects is provided. A review of rain cell signatures from former missions like SIR-C/X-SAR and the Shuttle Radar Topography Mission is given. Furthermore, the German spaceborne satellite TerraSAR-X delivered several measurements, which facilitate to study precipitation effects in SAR images. Based on these SAR images and simultaneously acquired weather radar measurements, a quantitative estimation of precipitation effects in SAR images is presented. In a further step, an attempt is made to extrapolate the effects observed in X-band SAR images to images acquired at higher nominal frequency bands such as Ka-band.

I. INTRODUCTION

The philosophy and intention of this article is to give first an introduction to the basic image formation concept of Synthetic Aperture Radar (SAR) and its diverse applications. Then we will focus on the specific aspects related to microwave propagation in the atmosphere. This will hopefully make the presented material beneficial for young scientists entering to the field. Experts from other domains not familiar with the basic concepts will hopefully also gain from the introduction, which is necessary in order to understand the context for the more recent findings treated afterwards. In the following we itemize the aspects which are covered in this tutorial article:

- Synthetic Aperture Radar basic image formation concept and applications
- Review of relevant propagation effects
- Probability of rain induced effects in X-band
- Physical interpretation of rain cell signatures in SAR images
- Modelling of rain cell signatures in SAR images
- Short summary and conclusions

II. ESSENTIAL BASICS OF SYNTHETIC APERTURE RADAR

Synthetic Aperture Radar represents a two-dimensional radar imaging technique based on active remote sensing of the Earth or other planets. In contrast to optical sensors, SAR is independent of day- and nighttime and can penetrate through clouds. However, as will be shown, SAR can be affected by propagation effects through heavy rain under adverse weather conditions. Nowadays, SAR is widely used for remote sensing of the Earth using air- and spaceborne platforms. Storage of the phase history allows for synthesis of a large synthetic aperture which improves the resolution in the azimuth direction tremendously. This can be illustrated by a simple example. A space-borne system operating in X-band with an antenna length of $12\,\mathrm{m}$, and altitude of $800\,\mathrm{km}$ would deliver only a poor resolution of $2000\,\mathrm{m}$ without using the synthetic aperture radar principle. However, with SAR the best achievable resolution that can be obtained is $D/2$, where D is the anntenna length. This result may seem astonishing since the resolution is independent of range.
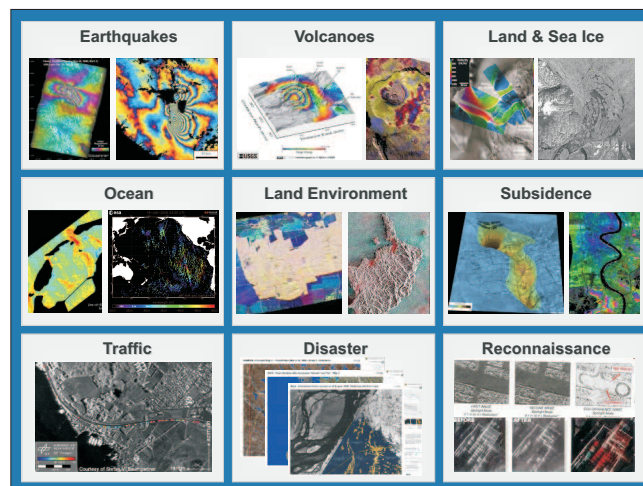

Fig. 1: A selection of applications for SAR (courtesy of G. Krieger).

The received radar signals contain information about roughness and geometrical structure as well as electrical properties of the imaged scene. Furthermore the signal may deliver information of the atmosphere and surface. Dependent on the wavelength also information of the subsurface can be gained.
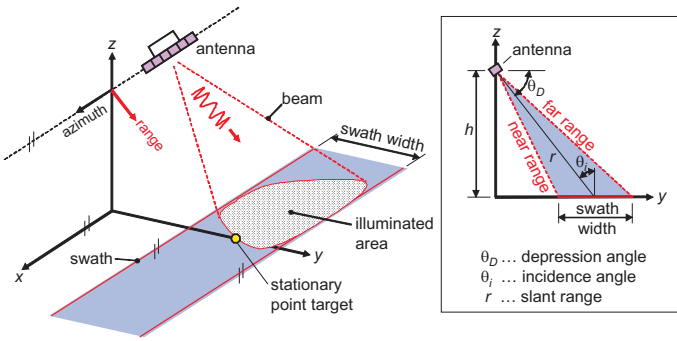
Fig. 2: A depiction of a SAR sidelooking imaging geometry.

Fig. 3: A flow chart of range Doppler imaging.

Radar imaging has been proven to be very successful for a wide range of remote sensing applications and some of them are exemplarily given in Fig. 1.

A typical SAR imaging geometry is given in Fig. 2, which shows a side-looking antenna mounted on a moving platform. Due to their higher altitude, satellite incidence angles vary less than airborne incidence angles. This leads to more uniform illumination on satellite images than for airborne radar images. We emphasize, that the velocity v of the platform carrying the antenna is small in comparison to the transmitted signals, which are propagating at a constant velocity equal to the speed of light ($c \approx 3 \times 10^8$ m/s). The antenna beam is pointing towards the earth and is illuminating the surface within the antenna footprint (intersection of beam with surface). The shaded area at the ground depicted in Fig. 2 is sometimes called the antenna footprint.

Note that the beam width is inversely proportional to the dimension of the antenna and the frequency, i.e. the larger the antenna and the higher the frequency, the smaller the beam width. The width of the so-called swath (ranging from near- to far range) limits the area of the surface which can be resolved in a processed SAR image in the across track dimension. The intersection of the vertical from the platform with the ground is called the *nadir*. In Fig. 2 the meaning of the depression- and incidence angle is shown.

The axis along the line of flight is called along-track or azimuth and the perpendicular direction is called in general range or across-track, where slant range and ground range have to be distinguished. The slant range denotes the distance from the aircraft to the scatterers, and the ground range the distance from the nadir to the observed scatterer. The term *squint* angle denotes the deviation angle between the main axis of the antenna beam and the plane perpendicular to the line of flight, where positive squint angles are by convention assigned to positive Doppler frequency shifts, and vice versa. We note that along-track and range directions are orthogonal to each other.

A. Image Formation Process

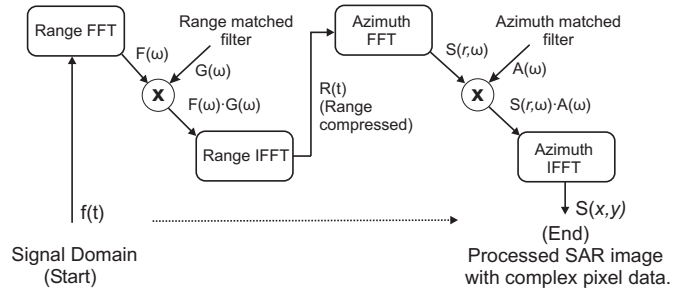As the platform moves along the azimuth direction the pulses are transmitted by the antenna with a certain pulse repetiton frequency (PRF). Instead of a short sharp pulse, a pulse having a large time-bandwidth product is transmitted. For obtaining a small range resolution and the highest possible signal-to-noise ratio pulse compression is carried out using a matched filter. The output or focused signal, respectively, is given by the convolution of the received signal with the reference signal/function. Following the optimal filter theory, the reference or matched filter function, respectively, is the complex conjugated and time-reverted function of the SAR system response.

The data collected by SAR systems are represented by a two-dimensional complex matrix in order to be processed to obtain a two-dimensional representation of the illuminated area.

An appropriate algorithm in order to understand the processing procedure is called either Range-Doppler or rectangular imaging [1] described in the following. The flow chart depicted in Fig. 3 shows the main required steps to transform from the raw time signal domain into the complex image domain.

The basic procedure of compressing the raw data in order to obtain an image is a two-dimensional correlation with a reference function, which is a matched filter operation.

The starting point for image processing after acquisition and sampling of the received analog data is the two-dimensional raw data matrix containing complex entries. The fundamental algorithm called 'rectangular' algorithm is briefly discussed. The algorithm is based on the rectangular assumption, assuming that the order of processing in range and azimuth is irrelevant and can be executed separately. The principle of compressing the raw data in range and azimuth via matched filter operations represents a well established and fundamental processing algorithm. We limit the treatment of processing algorithms herein. A variety of references are available cf. [1]–[6] that detail the subject more broadly.

Being a well established and matured remote sensing technique, a large body of literature exists for various topics of SAR imaging; reference is given to [7]–[11].

III. ASSESSMENT OF PROPAGATION EFFECTS IN SAR IMAGES

Amongst the many effects that may affect SAR images are delays, attenuation, noise, scintillation which are caused by atmospheric gases, rain (precipitation), clouds, fog or free electrons in the ionosphere.

Whether these effects are relevant depends on the signal parameters, the path geometry and the conditions prevailing in the ionosphere and the troposphere. The use of higher frequencies (X-band and beyond) minimises ionospheric effects on propagation, but tropospheric effects often increase or dominate as will be investigated in more detail.

The question to what extent atmospheric effects are critical depends also on the specific SAR application. For instance, for Synthetic aperture radar (SAR) interferometry, a powerful remote sensing technique for measuring the distance to the Earth's surface, the phase measurements is exploited. It requires that the surface is imaged by the radar at least twice from almost the same position in space. The differences in phase between the two images produce interferometric fringes that allows to deduce the topography of the surface. Any effect on the phase of the SAR signal will affect the accuracy of the height information. The focus in this contribution is mainly to the propagation effects that cause attenuation and backscattering in the image. For atmospheric effects on interferometric SAR techniques we refer to [12]–[14].

In the following some examples are shown how precipitation may affect SAR intensity images. The first example (Fig. 4) is taken from the SIR-C/X-SAR mission flown in 1994, where three images acquired in three different frequency bands are combined. The RGB-composite coding is (R) for X-band (G) for C-band, and (B) for L-band. As expected the "blocking" is most pronounced for X-band frequencies.

Three further examples of rain affected signatures in SAR images are given in Fig. 5 all of them taken from areas over tropical rain-forest, where heavy precipitation possesses highest probability on a world-wide scale.

For a recent measurement taken with TerraSAR-X, the German SAR satellite, launched in June 2007 and operating extremly successful since then [15], Fig. 6 is provided.

The physical processes are better elucidated with the help of Fig. 7 where a SAR amplitude cutout of cross-track profile through a rain cell is depicted. As diagrammatically shown, the backscattering is accompanied with higher amplitude values and the weak signals behind the first maxima belongs to the black shadows easily recognised in Fig. 7, where up to 20 dB difference in the dB level may be observed.

IV. TROPOSPHERIC EFFECTS

The troposphere, as the lowest part of the Earth's atmosphere, reaches from the surface to approximately 12 km above ground and causes, amongst other effects, attenuation of traversing signals due to hydrometeors (rain, snow, hail), atmospheric gases, fog and clouds [16]. Except at low elevation angles, the attenuation of frequencies below 1 GHz is negligible. Insignificant contributions to the attenuation will be obtained for frequencies up to 10 GHz due to fog and non-precipitating clouds. However the transmission spectrum exhibits peaks for frequencies around 22 GHz and 60 GHz due to molecular resonances from gases, i.e. water vapour and oxygen. Whereas absorption effects due to atmospheric gases are present constantly and everywhere, attenuation due to
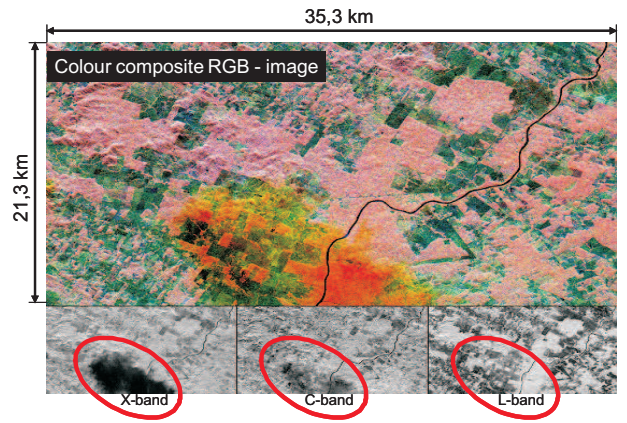

Fig. 4: Example of influence of rain on SAR intensity images, using the RGB composite corresponding to X-band (R), C-band (G), and L-band (B) measurements, respectively. The rain-induced 'blocking', as expected, is most pronounced in the X-band case. The images have been recorded during the X-SAR/SIR-C Mission conducted by DLR/NASA in 1994. The image is centered at 11.2° south latitude and 61.7° west longitude, respectively. North is toward the upper left.

condensed water in the form of precipitation, clouds and fog is infrequent and is limited to certain areas. Attenuation consists of two physical processes: the reduction of the wave's energy due to the heating of the water particles and, the scattering of energy away from the main direction of propagation.

A. Global Characteristics of Rain

On average, 50 % of the Earth's surface is coverered by clouds. However the rain to cloud ratio is seldom larger than 10 %. This means that the upper bound of 5 % on Earth's surface is receiving rain at a given time. Rain events are dominated by light rain events, however higher rain rates account for most of the total liquid water reaching the surface. Even for the areas with the highest rain rate, the percentage time in a year that exceeds 50 mm/hr is 0.1 % (annual probability) = 526 min. And 150 mm/hr is exceeded less than 0.01 % = 53 min.

B. Modelling of Attenuation and Backscattering in SAR Images

For the modelling of the attenuation and backscattering effects in SAR images, Fig. 8 is clarifying the underlying geometry [17]. The diagram provided at the bottom of Fig. 8 shows the qualitative variation of the normalised radar cross section (NRCS) due to the idealised rain cell. The detailed modelling and calculation is provided in the following two sections.

One of the major problems affecting microwave and millimetre wave bands for terrestrial and space-borne radars is the attenuation through rain [16]. A convenient way to describe the rain intensity is the so called rainfall-rate or rain-rate given in millimetres per hour. This quantity refers to a certain flux of rain towards the surface of the Earth and may be measured
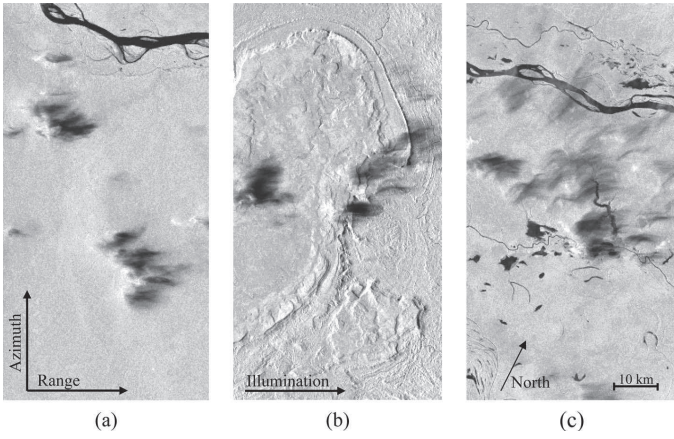
Fig. 5: Three examples of weather-corrupted SAR images from the SRTM mission (X-band: 9 GHz) from the Brazilian rain forest. The horizontal corresponds to range, and the vertical to the azimuth direction. The direction of illumination for all three images is given from the left- to the right-hand side. (a) DT: 087.070 Scene: 740. (b) DT: 150.050 Scene: 820. (c) DT: 039.070 Scene: 740.

Fig. 6: An example of a SAR image with rain-cell signatures recorded with TerraSAR–X in the US close to Baton Rouge. The white shading to the left of the dark spot is due to direct reflections from the rain region. The darkly shaded areas are due to rain attenuated (blocked) signals from the ground.

e.g. by gauges or weather radars. A widely acceped empirical relation of the form

$$\gamma(x,t) = a \cdot R^b \qquad (1)$$

between specific attenuation $\gamma(x,t)$ and rain rate R is used to calculate the specific attenuation for a given rain rate [16], [18]. The parameters a and b are dependent on the radio frequency, the raindrop size distribution, the polarization and other factors [18].

The total attenuation for a given instant of time can be obtained by adding up the specific attenuation along the path of propagation using the following expression [16]
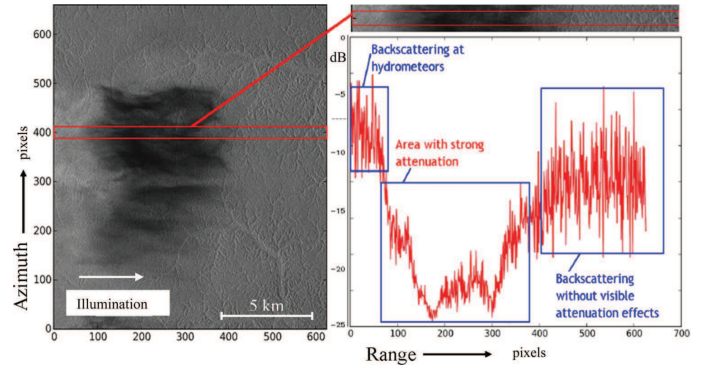

Fig. 7: Depiction of a slant-range reflectivity profile ("A-scope") for the rain-cell cut from a very recent TerraSAR-X measurement over a tropical rain forest in Brazil. Such data sets may, at some stage, enable estimation of rain rate over such isolated areas. This figure was inspired by the study of Runge et al. [19] who analyzed reflectivity profiles of SRTM data takes over a tropical rain forest.
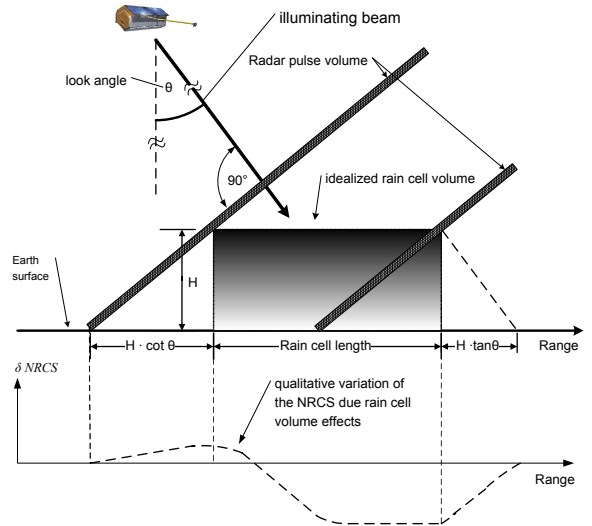

Fig. 8: A depiction of a SAR imaging scenario of an idealised rain cell. In the diagram the qualitative variation of the NRCS due to the rain cell volume effects is given. A combination of backscattering and attenaution can occur, where qualitatively the backscattering due to rain is the minor effect and attenuation the major [17].

$$A(t) = 2 \int_0^h \gamma(x,t)dx \qquad [dB] \qquad (2)$$

where

$A(t)$	... total attenuation for given time instant t
t	... time
h	... path length
$\gamma(x,t)$	... specific attenuation
x	... position along the path of propagation

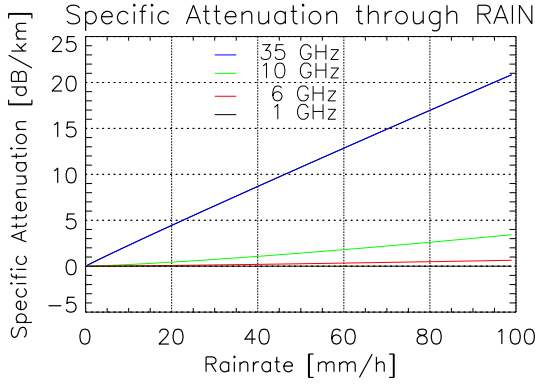The specific attenuation along the slant path of propagation

Fig. 9: A plot of the specific attenuation given in units of dB/km versus the rain rate in units of mm/h for four different frequencies (1, 6, 10 and 35 GHz) after [21].

has to be known. However, detailed knowledge of the medium through which the signal propagates is rather limited and the temporal and spatial variation of the medium require assumptions and some modelling. In the case of precipitation we may have some idea about the thermodynamic phase (ice, water, melting band) but no precise information. Using the calculated values for the specific attenuation in X-band provided in diagram Fig. 9 for a 5 km long path through a heavy tropical convective rain (70 mm/h and more) suggests a 20 – 30 dB two-way attenuation, which was confirmed by comparing the backscattering coefficient of affected and non-affected region from data takes acquired by TerraSAR-X over Brazilien rain forest [20].

C. Modelling of the Attenuation under Rain Conditions for Ka-band

For the calculations of the rain rate to cause visible attenuation in Ka-band SAR images, a simple model shown in Fig. 10 [17], is used. A reasonable height of 4 km is assumed, as well as a homogenous rain rate for the modelled cell. The incidence angle of the propagating signals was chosen 30°. With the help of (1) and by using the regression coefficients in Table I, the specific attenuation was calculated. These values are given in Table II. Finally, the values for the two-way path attenuation for different rain rates (5, 50 and 100 mm/h) can be found in Table III.

As a total two-way attenuation of 25 dB becomes visible in SAR images in X-band it is of interest which rain rate is necessary to cause such an attenuation for Ka-band (35 GHz) frequencies. To this end, the following equation is applied

$$\gamma(t) = \frac{A(t)}{2 \cdot \frac{H}{\cos(\theta)}} \qquad \text{[dB/km]}, \tag{3}$$

where the rain rate is found using (1) with the according parameters a and b for Ka-band

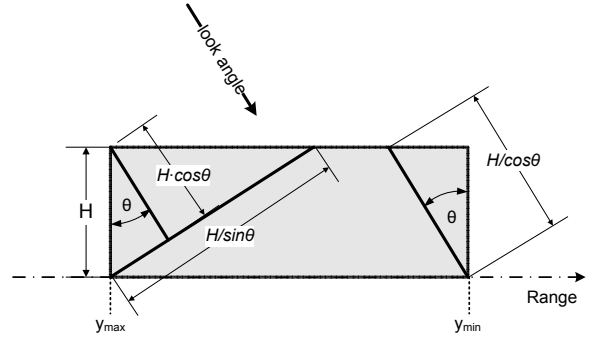$$R = \sqrt[b]{\frac{\gamma(t)}{a}}. \tag{4}$$

Fig. 10: The structure of an idealised rain cell used for the calculation in Section IV-C.

TABLE I: Regression coefficients used for the calculation of the specific attenuation cf. (1)

| Frequency | DSD | | | |
| | Mar. Palmer | | Joss Thunderst. | |
	a	b	a	b
X-Band (10 GHz)	0.0136	1.15	0.0169	1.076
Ka-Band (35 GHz)	0.268	1.007	0.372	0.783

First calculations using the parameters of the idealised rain cell of 4 km and using 25 dB of total two-way attenuation, assuming the Marshall Palmer Parameters for Ka-band attenuation deliver a rain rate close to 10 mm/h. This simple example demonstrates that such rain rates are fully capable to distort Ka-band SAR measurements to a visible extent. In Fig. 11 the range of values for attenuation and rain rate are extended and the diagram shows the two-way attenuation versus the rain rate for different incidence angles at Ka-band. Similar information is provided for X-band frequencies in Fig. 12 for comparison. The aforementioned simple assumptions of a homogenous rain

TABLE II: Specific Attenuation [dB/km]

| Rainrate [mm/h] | Specific Attenuation | |
	10 GHz	35 GHz
5	0.08	1.31
50	1.22	7.95
100	2.4	13.69

TABLE III: Maximum attenuation for modelled rain cell [dB].

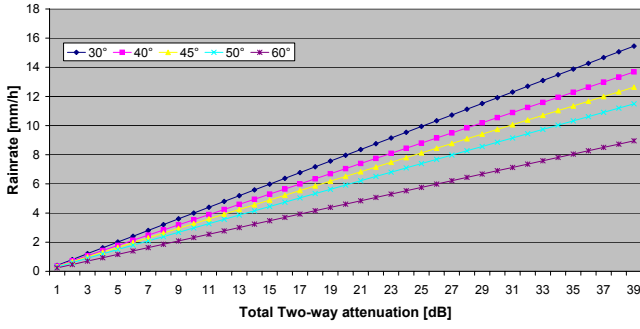| Rainrate [mm/h] | Specific Attenuation | |
	10 GHz	35 GHz
5	0.739	12.1
50	11.26	73.43
100	22.17	126.46

Fig. 11: A diagram of the two-way path attenuation and the corresponding rain rate for the modelled rain cell of 4 km height (Fig. 10) at Ka-band (35 GHz), for different look angles.
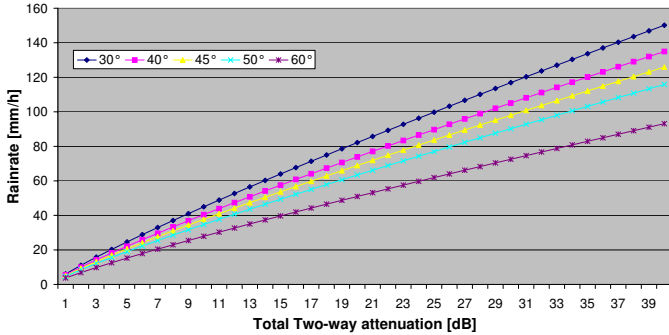

Fig. 12: A diagram of the two-way path attenuation and the corresponding rain rate for the modelled rain cell (Fig. 10) at X-band (10 GHz), for different look angles.

cell with constant precipitation may be somehow optimistic, since a melting layer precipitation may severly increase the total path attenuation.

D. Consideration of Backscattering Effects in SAR Imaging

The radar response (backscattering) from hydrometeors is determined by the raindrop size, shape, density, orientation, and temperature. Furthermore, the backscattering depends on the polarization of the wave interacting with the precipitation media. The theoretical concept that describes the scattering from a dielectric sphere was established by Mie in 1908. The relation to estimate the backscatter cross section of a volume of small particles by assuming the well-known Rayleigh approximation (the diameters D of the raindrops are much smaller than the wavelength λ) is given as [23]

$$\sigma_b = \frac{\pi^5}{\lambda^4} |K|^2 \sum_{i=1}^{N} D_i^6 \qquad (5)$$

where

$$K = \frac{m^2 - 1}{m^2 + 2} \qquad (6)$$

and m is the complex index of refraction of the scattering

particle. The summation term for a distribution of particles can be given as

$$\hat{Z} = \int N(D_e) D_e^6 dD_e \qquad [mm^6/m^3], \qquad (7)$$

where $\hat{Z}$ is termed the reflectivity factor, D_e is the diameter of each droplet and $N(D_e)$ is the number of droplets per unit volume.

$$N(D_e) = N_0 e^{-\lambda_d D_e}, \quad \lambda_d = 4.1 \cdot R^{-0.21} \qquad (8)$$

where N_0 and λ_d are the parameters defining the drop size distribution (DSD). For the special case of the Marshall-Palmer distribution the parameter N_0 is given as 8000 in m^{-3} mm^{-1} and λ_d [mm^{-1}] is related to the rainfall intensity R [mm/h] as shown in Eq. (8).

Note that $\hat{Z}$ is commonly given in logarithmic units according to

$$Z = 10 \cdot log_{10} \hat{Z} \qquad [dBZ]. \qquad (9)$$

As a practical basis for estimating the precipitation intensity directly from the measured reflectivity factor in still air, the following relation is used

$$\hat{Z} = a_1 \cdot R^{b_1}. \qquad (10)$$

The parameters a_1 and b_1 are dependent on the frequency of the interacting EM waves and on the rain intensity R as well as the DSD. Furthermore, regional-dependent variations due the rain type do exist. A number of $Z - R$ relations were established by many research efforts and are provided, for instance, in [18]. A careful selection of the coefficients has to be performed by considering the appropriate conditions and respective parameters.

The power law in (10) provides an analogy to the calculations of the specific attenuation using (1) given in Section IV-C.

For a further in-depth analysis of the theoretical aspects of backscattering due to hydrometeors, we refer to [24]. For the case of SAR, it can be concluded that the backscattering due to hydrometeors is the minor effect and attenuation due to the precipitation volume is dominating, which is supported by the recent measurements of TerraSAR-X.

It has been observed that backscattering due to precipitation can easily enhance the backscattering about 5 dB compared to unaffected regions of the image.

E. Test Case and Comparison of SAR Data with Simultaneously Measured Ground-based Weather Radar Data

Fig. 13 shows a comparison of two different types of images measured almost at the same time, where the image on the left-hand side was acquired with TerraSAR-X [15] strip-map mode in ascending orbit over New York. The image on the right-hand side displays the corresponding weather radar image measured by a ground-based weather radar (WSR-88D) located in New York (Nexrad code: KOKX). The data were obtained using

the freely available Java NEXRAD viewer provided by the National Oceanic and Atmospheric Administration, U.S. A good agreement between visible artifacts shown in the SAR image (some of them encircled in red color) and the reflectivity plot on the right-hand side was observed. Such reflectivity maps display the echo intensity of the transmitted radar signals and are shown in dBZ. These maps are used to detect precipitation and evaluate storm structures. It is the best available means to compare precipitation volumes and precipitation-induced signatures in SAR images. The reason lies in the high achievable spatial resolution and the possibility to measure at almost the same instant of time. The red regions in the weather radar image correspond to reflectivities up to 50, in some cases 55 dBZ, which corresponds to high precipitation intensities typically occurring during thunderstorms. The comparison of ground-based weather radar and SAR data will be certainly useful in the process to derive rainintensity information from SAR-based measurements.

V. IDENTIFICATION OF MEASURES AND RECOMMENDATION TO COUNTERACT AND/OR ENHANCE PRECIPITATION EFFECTS ON SAR

In this section we briefly highlight some of the possibilities to overcome the limitations of the SAR system under investigation due to adverse meteorological conditions. The ideal strategy to identify rain induced signatures would be a multi-frequency SAR system, because attenuation through rain is wavelength dependent. Since current SAR systems are not equipped with such a multi frequency sensor set, other ways have to be taken into consideration. Wherever available, ground based weather radar would assist in the process to identify precipitation induced distortions in SAR images. However, world-wide coverage of ground based weather radars is limited to industrialized regions such as the USA or Europe. Especially over the oceanic regions no ground based weather radar data are available and so it is for the polar regions of the Earth. One simple measure to avoid or mitigate precipitation effects are multi-temporal acquisitions over the same scene, since the statistical probability for rain is rather low, as already shown before. As the look angle determines the path length of the propagation path through the precipitation media, steep look angles would reduce the attenuation due to rain, and conversely shallow look angles cause increased values of attenuation. The question to what extent scan-on-receive techniques are capable to improve, respectively enhance precipitation effects was addressed by [22], and deserves further consideration. A mitigation of the backscattering can be obtained. However, the attenuation will still be present for transmit and receive patterns as is diagrammatically shown in Fig. 14.

VI. CONCLUSIONS

A brief introduction to the SAR imaging concept was given followed by a discussion of propagation distortions and their influence on the image quality. Propagation effects can be very important and need to be considered in interpreting radar images. It has been shown that attenuation due to rain
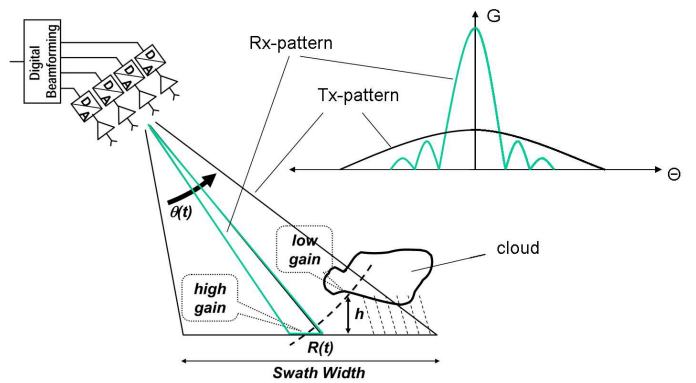

Fig. 14: A depiction of an imaging scenario with scan-on-receive technique. The different gain in receive Rx (pencil beam) and Tx allows for an improvement of the SNR in the presence of rain for backscattering. However, the attenuation can not be avoided.

is the dominating effect, together with backscattering from precipitation at higher frequency bands such as X- and Ka-band. Since the effects of backscattering and attenuation are interconnected to each other it is sufficient to consider at least the major disturbance (=attenuation through rain) in order to flag an affected SAR image. A model to quantify propagation effects in SAR images has been presented, which allows for a quantitative assessment of the pertinent effects. Depending on the climatic region on Earth, the availability of a Ka-band system will vary. Assuming a 5 dB acceptance of the attenuation due to rain, which corresponds to 2 mm/h at $30°$ incidence angle for the modelled rain cell used in this paper, the availability will be better than 98 % for the European regions and better than 95 % for rain-forest in Brazil. Clouds with little water liquid content, low rain rates and homogenous distribution will cause no or only little disturbance (visible artefacts). The disadvantage of rain cell signatures might offer the potential advantage to derive meteorological information.

VII. ACKNOWLEDGEMENTS

REFERENCES

[1] W. G. Carrara, R. S. Goodman, and R. M. Majewski. *Spotlight Synthetic Aperture Radar: Signal Processing algorithms*. Artech House, 1995.
[2] I. Cumming and F. Wong. *Digital Processing of SAR Data*. Artech House, Norwood, MA, 2005.
[3] J. C. Curlander and R. N. McDonough. *Synthetic Aperture Radar: Systems and Signal Processing*. J. Wiley and Sons, New York, 1991.
[4] M. Soumekh. *Synthetic Aperture Radar Signal Processing with MATLAB Algorithms*. Wiley, 1999
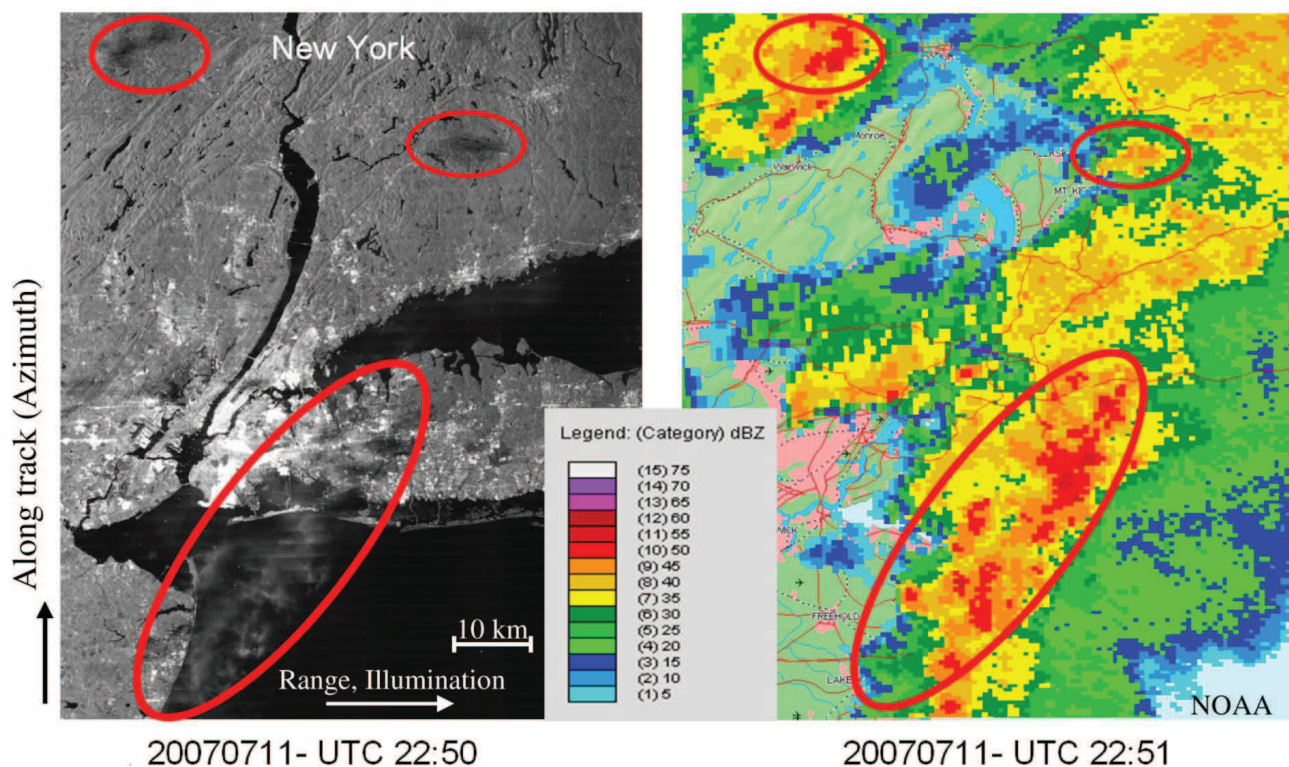[5] J. P. Fitch. *Synthetic Aperture Radar*. Springer Verlag, 1988.

Fig. 13: Test case showing a comparison of TerraSAR-X and weather radar data acquired nearly simultaneously (within the same minute) over New York, U.S. A good agreement between the rain-cell signatures in (left) the SAR image and (right) the weather radar image can be observed. The effects are most pronounced for reflectivities of up to 50 dBZ. The SAR image was acquired in ascending orbit direction, and the range direction corresponds with the horizontal. The look direction was from left to right. The vertical corresponds to the along-track direction. Image dimensions are approximately 130 km in azimuth and 100 km in range direction.

[6] H. Klausing and W. Holpp, editors. *Radar mit realer und synthetischer Apertur*. Oldenburg, München, Wien, 2000.

[7] C. Oliver and S. Quegan. *Understanding Synthetic Aperture Radar Images*. Sci Tech, Raleigh, NC, 2004.

[8] F. M. Henderson and A. J. Lewis, editors. *Manual of Remote Sensing, Principles and Applications of Imaging Radar*. Wiley, 1998.

[9] C. Elachi and J. J. van Zyl. *Introduction to the Physics and Techniques of Remote Sensing*. Wiley, 05 2006.

[10] H. Mott. *Remote Sensing with Polarimetric Radar*. Wiley, 2007.

[11] J. S. Lee and E. Pottier. *Polarimetric Radar Remote Sensing*. CRC Press, 2009.

[12] R. F. Hanssen. *Radar Interferometry: Data Interpretation and Error Analysis*. Kluwer Academics, 2001.

[13] H. A. Zebker, P. A. Rosen, and S. Hensley. "Atmospheric Effects in Interferometric Synthetic Aperture Radar Surface Deformation and Topgraphic Maps." *Journal of Geophysical Research*, 102:7547–7452, 1997.

[14] A. Danklmayer, E. Archibald, T. Boerner, D. Hounam, and M. Chandra. "Atmospheric Effects and Product Quality in the Application of SAR Interferometry." In: *Proceedings of EUSAR 2004*, Ulm, Germany. ISBN 3-8007-2828-1.

[15] R. Werninghaus, St. Buckreuss, "The TerraSAR-X Mission and System Design" *IEEE Transaction on Geoscience and Remote Sensing*, accepted for publication in a Special issue on TerraSAR-X; available online [http://ieeexplore.ieee.org]; in hard copy to appear in 2010.

[16] R. K. Crane, *Electromagnetic Wave Propagation through Rain*. John Wiley and Sons, 1996.

[17] C. Melsheimer, *Signaturen von Regen in Radaraufnahmen des Meeres*. Aachen: Shaker Verlag, 1998.

[18] R. L. Olsen, D. V. Rogers, and D. B. Hodge. "The $a \cdot R^b$ Relation in Calculation of Rain Attenuation," *IEEE Transactions on Antennas and Propagation*, vol. 26, no. 2, pp. 318–329, 1978.

[19] H. Runge, S. Cloude, M. Eineder, A. Fusco, E. Gill, I. Hajnsek, C. Heer, F. Jochim, M. Kirschner, G. Krieger, A. Moreira, T. Niederstadt, K. Papathanassiou, R. Romeiser, R. Scheiber, C. Sickinger, and S. Suchandt. *New Techniques for Simultaneous SAR Interferometry* Eur. Space Agency, Noordwijk, The Netherlands, Final Rep. ESA Contract 16100/02/NL/EC, 2003.

[20] A. Danklmayer, B. Döring, M. Schwerdt, and M. Chandra. "Assessment of Atmospheric Effects in SAR Images," *IEEE Transaction on Geoscience and Remote Sensing*, 2009, vol. 47, no. 10, pp. 3507-3518, October 2009,

[21] Specific Attenuation Model for Rain for Use in Prediction Methods, 2005. *ITU-Recommendation P. 838-3.*

[22] S. D'Addio, M. Ludwig, "Rain Impact on Sensitivity of Ka-band Scan-on-Receive Synthetic Aperture Radars," in *IEEE International Geoscience and Remote Sensing Symposium, (IGARSS)* 2008, vol 3, 7-11 July 2008 Page(s):III - 1174 - III - 1177, Boston, US

[23] V. N. Bringi and V. Chandrasekar. *"Polarimetric Doppler Weather Radar, Principles and Applications"*, Cambridge University Press, New York, 2001.

[24] T. Oguchi, "Electromagnetic Wave Propagation and Scattering in Rain and other Hydrometeors," *Proc. IEEE*, vol. 71. no. 9, pp. 1029-1078, Sep. 1983